Impact of cationic vacancies on the physical characteristics of multiferroic $GdMnO_3$

A. Pal, and P. Murugavel

Citation: Journal of Applied Physics **123**, 234102 (2018); doi: 10.1063/1.5029509
View online: https://doi.org/10.1063/1.5029509
View Table of Contents: http://aip.scitation.org/toc/jap/123/23
Published by the American Institute of Physics

Impact of cationic vacancies on the physical characteristics of multiferroic $GdMnO_3$

A. Pal and P. Murugavel[a)]
Department of Physics, Indian Institute of Technology Madras, Chennai 600036, India

(Received 15 March 2018; accepted 31 May 2018; published online 19 June 2018)

The effects of cationic vacancies on the structural, dielectric, and magnetic properties are investigated in polycrystalline $GdMnO_3$ samples. Samples with reduced cationic vacancies are synthesized by annealing under the forming gas atmosphere. The x-ray photoelectron spectroscopy studies show evidence for excess oxygen in terms of the Mn^{4+} content and reveal the increase in the Mn^{3+}/Mn^{4+} ratio with increase in annealing time under forming gas conditions. Dielectric studies reveal two thermally activated relaxations in the low and high temperature regimes. Notably, the near stoichiometric Mn^{3+} rich samples show a negative temperature coefficient of ac conductivity in a certain temperature region along with better insulating properties. The magnetic measurements exhibit a gradual increase in the onset of weak ferromagnetic transition temperature with increase in the Mn^{3+} content in the sample and coincides with the Neel temperature (42 K) near stoichiometric composition. The studies demonstrate the effect of subtle change in oxygen non-stoichiometry on the dielectric and magnetic properties and bring out the importance of controlling stoichiometry in $GdMnO_3$. *Published by AIP Publishing*. https://doi.org/10.1063/1.5029509

I. INTRODUCTION

Rare earth manganites ($RMnO_3$, R = rare earth ion) have gained considerable interest due to their complex magnetic orderings associated with intriguing physics and application potentials in multifunctional devices.[1–3] They are known for their unusual magnetoresistance and magnetodielectric (MD) properties.[4–8] Interestingly, the physical properties of these systems can be vastly altered by alkaline earth metal ion (Ca, Sr or Ba)[6,9–11] and/or transition metal ion (Fe, Cr) substitutions[12–15] on the R-site or Mn-site. However, the deviation from stoichiometry is one of the major issues which makes it difficult to control the physical properties of these systems. The $RMnO_3$ with larger R-ionic radii is proven to show a large oxygen non-stoichiometry.[16–19] As an example, though the stoichiometric $LaMnO_3$ is an antiferromagnetic (AFM) insulator, the synthesized compound under the ambient condition always yields ferromagnetic (FM) insulator/metallic characteristics.[17–20] This change in properties is mostly attributed to excess oxygen in the perovskite system and the resultant charge imbalance can be partially compensated by the oxidation of Mn^{3+} to Mn^{4+} at the B-site or by La-ion vacancy at the A-site (note that the excess oxygen in perovskite means equal distribution of A and B-site cationic vacancies).[16,17,20] However, the $RMnO_3$ system with lower R ionic radius with more stability in the crystal structure is generally believed to be in the oxygen stoichiometric state.[17,19] As a result, the effect of oxygen non-stoichiometry has rarely been investigated on other $RMnO_3$ systems.

Recently, $GdMnO_3$ (GMO) has gained importance due to the coexistence of ferroelectric and magnetic orderings with the resultant large MD effect.[7,8,21] Here, Mn^{3+} moments undergo an incommensurate sinusoidal AFM ordering at T_N (~42 K) followed by a canted magnetic phase transition at T_{lock} (~23 K) below which a ferroelectric state appears due to spin canting in the system.[22,23] This results in numerous reports on the investigations of both dielectric and magnetic properties of GMO in the region confined to below 50 K.[7,8,22–25] Most of these studies presumed GMO in the stoichiometric state and hence overlooked the effect of oxygen non-stoichiometry on such important properties.[22,24,25] Note that the presence of defect dipoles and trapped charges originated from cationic vacancies reported to show additional pyroelectric signals well above ferroelectric transition in the GMO sample.[26,27] Such cationic vacancy in GMO can originate from the oxygen non-stoichiometry. The resultant Mn^{3+}-Mn^{4+} may alter the magnetic state of the sample by Zener double exchange (DE) interaction along with its conduction properties through small polaron hopping.

To investigate it in detail, the GMO samples with variation in oxygen stoichiometry are synthesized under the oxygen reduced forming gas atmospheric annealing condition and subjected to structural, dielectric, impedance, and magnetic studies. The structural studies reveal a oxygen non-stoichiometric state in ambient annealed samples as compared to the samples annealed under reducing conditions which show a near stoichiometric state. In addition, the dielectric and impedance studies exhibit enhancement in the insulating character when the samples move towards the stoichiometric state with increase in annealing time under the reduced condition. Interestingly, a pronounced change in magnetic ordering temperature and possible spin structure for samples with different annealing times can be corroborated from the magnetic measurements. The detailed discussion will be presented in this work.

II. EXPERIMENTAL DETAILS

Polycrystalline samples of $GdMnO_3$ were prepared by the solid state synthesis method. Initially, a stoichiometric amount of Gd_2O_3 (pre-heated at 1000 °C for 12 h) and

a)Author to whom correspondence should be addressed: muruga@iitm.ac.in

Mn_2O_3 precursors were mixed, ground in an agate mortar, and calcined at 1000 °C for 24 h in air followed by several intermittant grinding and heating steps at 1100, 1200, and 1300 °C for 24 h each. The pellets of uniaxially pressed calcined powder were sintered at 1350 °C for 24 h in air to achieve high density (>95% of theoretical density). This sample is hereafter called as G1. The sintered pellets were then subjected to additional heat treatment at 1350 °C for 15 min, 30 min, 45 min, and 1 h in an oxygen reduced (forming gas) atmosphere (95% N_2 + 5% H_2) and they are called as G2, G3, G4, and G5, respectively. The x-ray powder diffraction (XRD) data were collected with a PANalytical x-ray diffractometer and x-ray photoelectron spectroscopy (XPS) was performed using a Omicron ESCA+ (Oxford Instruments, Germany) system at room temperature. Dielectric measurements were carried out with Novocontrol Alpha-analyzer in the temperature range of 123–573 K at various frequencies from 10 Hz to 20 MHz. Magnetic measurements were performed with a SQUID magnetometer (Quantum Design, USA) in the 5–360 K temperature range at -7 T to 7 T applied magnetic field. For dielectric measurements, electrodes were made on both surfaces of the pellet using silver paint.

III. RESULTS AND DISCUSSION

A. XRD studies

To confirm the phase formation and study the structural details, the XRD experiment is performed on the samples and the XRD patterns are shown in Fig. 1(a). The patterns reveal the phase pure formation of the compound and the peaks are all indexed to the orthorhombic structure with the *Pnma* space group. In addition, the diffraction peaks show a systematic shift towards a lower diffraction angle with increase in the forming gas annealing time. To extract the structural parameters, the diffraction patterns are fitted with Rietveld refinement using the GSAS software. The low values of observed profile parameters such as goodness of fit (χ^2) and weighted profile R factor (R_{wp}) indicate the best fit. For example, χ^2 and R_{wp} values are 1.23% and 2.13%, respectively, for sample G3. The extracted lattice parameters are plotted in Fig. 1(b) as a function of annealing time. The figure reveals the monotonous increase in lattice parameters with increase in forming gas annealing time. In the absence of any secondary phases, the increase in lattice parameters and thereby the increase in volume can be understood from the change in the average Mn-site ionic radius arising out of its mixed valence state. The ionic radius of Mn^{3+} (0.645 Å) being greater than the ionic radius of Mn^{4+} (0.53 Å) strongly indicates that the increase in forming gas annealing time brings out the gradual conversion of Mn^{4+} into Mn^{3+} and thereby results in an increase in lattice parameters.[19,28] Despite the fact that all samples are crystallized in the O'-type ($b/\sqrt{2} < c < a$) orthorhombic structure,[29] the increasing separation between the lattice parameters with annealing time could be associated with the increasing Jahn-Teller (JT) distortion in the samples. This gives an additional support for the increase in Mn^{3+} ions with annealing time as Mn^{3+} ($3d^4$) is considered as JT active, whereas Mn^{4+} ($3d^3$) is JT inactive.

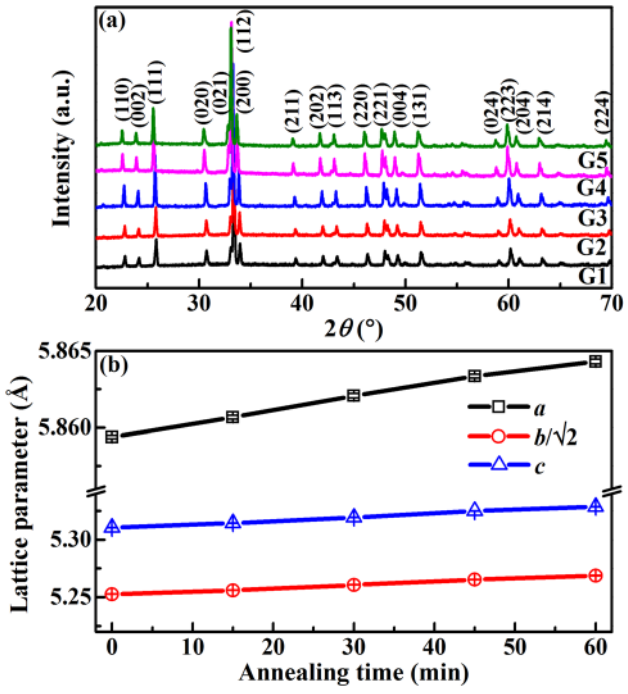

FIG. 1. (a) XRD patterns of all samples annealed in the oxygen reduced atmosphere and (b) variation of lattice parameters as a function of annealing time.

B. XPS studies

To confirm the mixed valence state of the Mn ion, the core level XPS experiment is performed on selective samples such as G1, G3, and G5 at room temperature. The obtained XPS Mn $2p_{3/2}$ peaks for G1, G3, and G5 are shown in Figs. 2(a), 2(b), and 2(c), respectively. The peak fitting done after appropriate background subtraction along with two deconvoluted peaks, assigned to Mn^{3+} and Mn^{4+} ions, is shown in Fig. 2. Note that the binding energies of Mn^{3+} and Mn^{4+} ions in the $2p_{3/2}$ spectrum are in the range of 640–640.8 eV and 642.1–642.5 eV, respectively.[19,30] The figure shows that the $2p_{3/2}$ peak is shifting towards lower binding energy with increase in annealing time. This reveals the change in the Mn^{3+}/Mn^{4+} ratio among samples and its increasing trend with annealing time. It can be further confirmed from the area under the Mn^{3+} (Mn^{4+}) peak which shows an increase (decrease) in trend from sample G1 to G5. Overall, the XPS studies confirm the presence of the mixed valence Mn-ionic state in ambient annealed sample G1 and the near stoichiometric nature for the sample annealed under forming gas for 1 h (G5).

C. Dielectric properties

In order to understand the dielectric properties of the samples, the dielectric constant (ε_r') is measured as a function of temperature at different frequencies from 10 kHz to 1 MHz and the results are plotted in Figs. 3(a)–3(e). The ε_r' for sample G1 shows two broad humps in the temperature range from 200–350 K and 400–550 K. They are named as T_1 and T_2 as indicated in Fig. 3(a). The ε_r' displays frequency

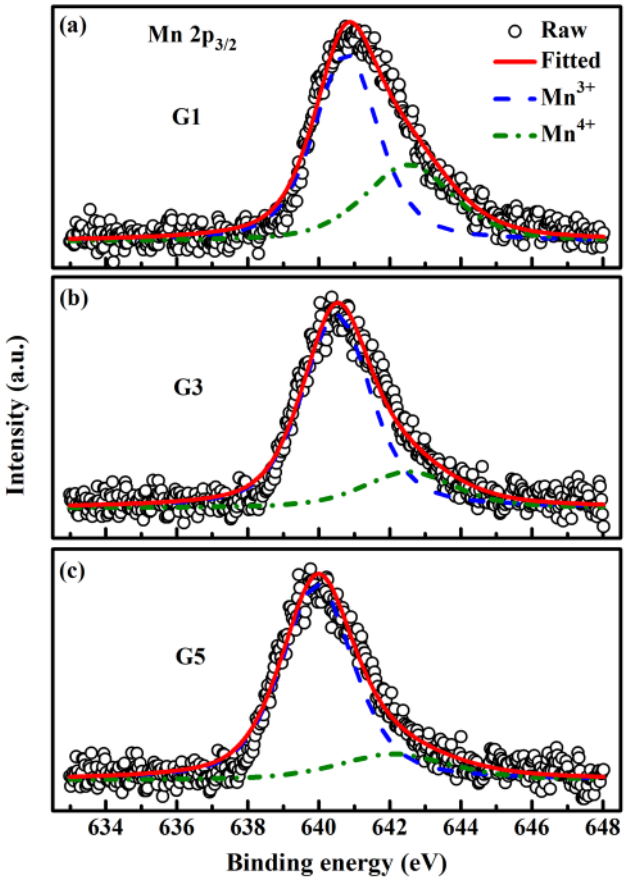

FIG. 2. XPS plots for Mn $2p_{3/2}$ of samples (a) G1, (b) G3, and (c) G5, at room temperature.

independent behaviour below 200 K and thereafter shows frequency dispersion. The ε_r' increases with temperature and the observed maxima at T_1 shifts to the higher temperature with increasing frequency suggesting the thermally activated relaxor behaviour in the 200–350 K range. With further increase in temperature, an additional relaxation phenomenon is observed at T_2. However, with increase in annealing time, Fig. 3 reveals the decreasing trend of ε_r'. In addition, the relaxations observed at T_1 and T_2 shift towards higher temperature as evidenced from the sample G2. As a consequence, the samples G3, G4, and G5 show the signature of relaxation at T_1 shifting towards high temperature. However, the appearance of an additional relaxation at the low temperature (T_3) side could be correlated to the trapped charges from the localized Mn sites.[26,27] This trend is clearly visible in Fig. 3(f), where temperature dependent ε_r' is plotted at 10.8 kHz for all samples.

D. Conductivity studies

To understand the origin of these relaxation phenomena, we have plotted the ac conductivity ($\sigma_{ac} = \varepsilon_0 \varepsilon_r' \omega \tan\delta$, where ε_0 is the permittivity in free space, ω is the frequency, and $\tan\delta$ is the dielectric loss) versus $1000/T$ at different frequencies for all samples in Figs. 4(a)–4(d). The figure reveals three distinct regions, marked as region I, region II, and region III in Fig. 4, suggesting their origin to different conduction mechanisms. In region I (low temperature), the conductivity displays frequency dependent characteristics and becomes nearly frequency independent in region III (high temperature) for all the samples. It is noteworthy to mention

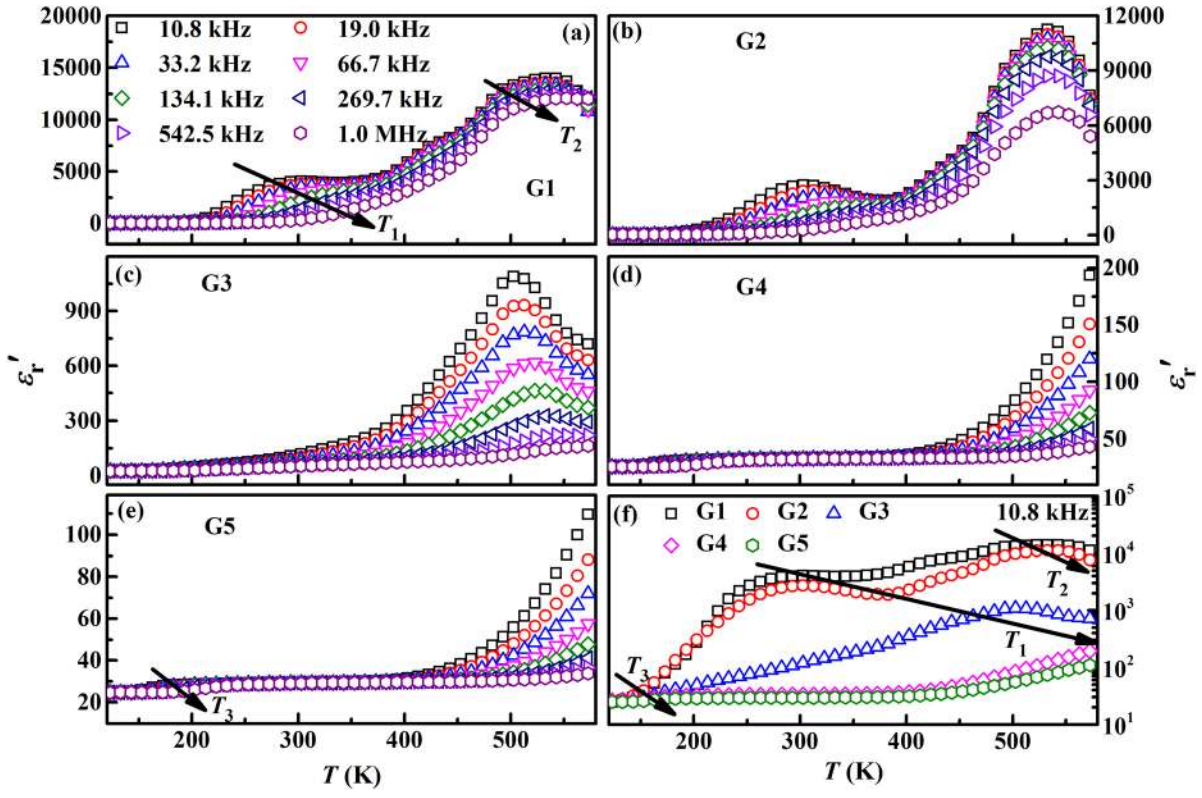

FIG. 3. (a)–(e) Temperature dependence of dielectric constant at different frequencies for all samples and (f) comparison of the temperature dependent dielectric spectra of all samples at 10.8 kHz.

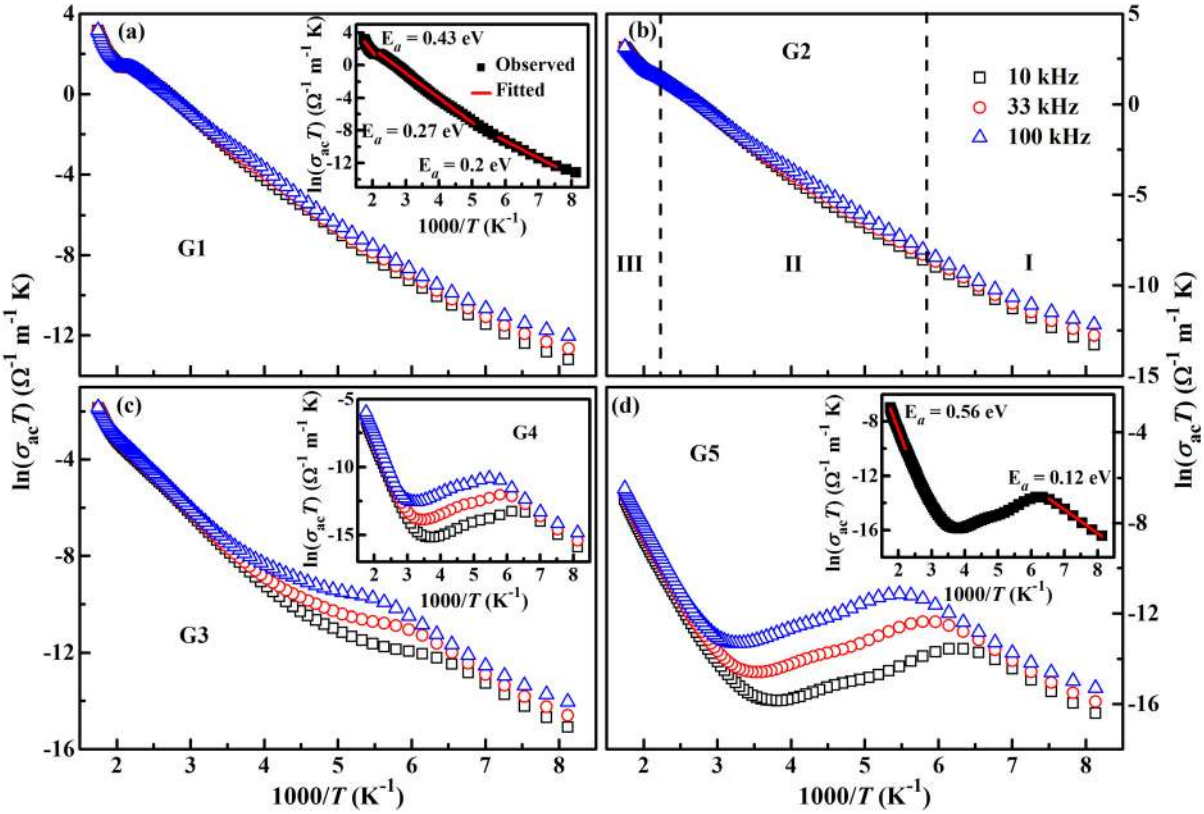

FIG. 4. Plot of $\ln(\sigma_{ac}T)$ versus $1000/T$ at different frequencies for samples (a) G1, (b) G2, (c) G3, and (d) G5. The inset of (c) shows the respective plot for sample G4 and the insets of (a) and (d) show the linear fitting using the small polaron hopping model for samples G1 and G5, respectively.

that though the samples show the positive temperature coefficient of conductivity in region I and III, the samples G4 and G5 exhibit an unusual negative temperature coefficient of conductivity (NTCC) in region II. The temperature range in which the NTCC appearing shows an increasing trend with annealing time along with its dispersion with frequency as evidenced from Figs. 4(c) and 4(d). Note that the conductivity decreases with increase in annealing time along with the decrease in tan δ (not shown in the figure).

The activation energies for the conduction in these regions may give an insight regarding the origin of these regions. For this purpose, the ac conductivity data shown in Fig. 4 are fitted with the Arrhenius like equation given by Mott and Davis for the phonon-assisted hopping model[15,31] namely $\sigma_{ac}T = \sigma_0 \exp\left(-\frac{E_a}{k_B T}\right)$, where, σ_0 is the pre-exponential factor, E_a is the activation energy for conduction, and k_B is the Boltzmann constant. As a representative example, the fitted data are shown as insets in Figs. 4(a) and 4(d) for G1 and G5, respectively.

The extracted E_a values are tabulated in Table I and they are in the range of 0.12–0.56 eV. Note that the fitting is not done in region II (NTCC region) as it is a thermally deactivated region with no potential barrier. The observed values of E_a being around 0.12 eV in region I may indicate that the conductivity mechanism arises due to trapped charges from the localized Mn sites,[26] while the values of E_a being around 0.5 eV in region III are well in agreement with the reported values for hopping conductivity.[15,32,33] The competition between these two relaxation mechanisms may introduce the NTCC region in the intermediate temperature range in G4 and G5. Note that oxygen non-stoichiometry is a known issue in orthorhombic $R\mathrm{MnO_3}$ and the resultant cationic vacancies in these compounds can lead to Mn^{3+} and Mn^{4+} mixed valence states.[10,34] Consequently, the holes created during $Mn^{3+} \rightarrow Mn^{4+}$ transformation can be localized at Mn-sites as a small polaron.[15,33,35] Hence, the resultant p-type conduction mechanism will be dominated by the thermally activated hopping of small polarons between Mn^{3+} and Mn^{4+} sites for all samples. In polycrystalline samples, the hopping of such small polarons can cause a distinctly different effect depending on the temperature range. At low temperature, such hopping between spatially fluctuating lattice potentials inside the grain may give rise to the dipolar effect, while the possibility of hopping in the vicinity of blocking grain boundaries may result in the formation of space charges at high temperature. The giant dielectric constant at

TABLE I. Activation energy for ac conductivity obtained from the small polaron hopping mechanism in different temperature regimes.

	E_a (eV)		
Sample	Region-I	Region-II	Region-III
G1	0.13	0.27	0.43
G2	0.13	0.28	0.44
G3	0.13	…	0.48
G4	0.12	…	0.54
G5	0.12	…	0.56

high temperature may be due to the relaxation of these space charges at the interfacial grain boundary sites.[36]

E. Impedance studies

To understand the effect of grain and grain boundary on hopping conductivity, the impedance analysis is performed on all samples. The real part of the impedance (Z') plotted as a function of $-Z''/f$, where Z'' is the imaginary part of the impedance and f is the frequency, at 323 K for G1, G3, and G5 are shown in Figs. 5(a), 5(b) and 5(c), respectively. The insets show the respective plots at 223 K. The temperatures 223 K and 323 K are chosen according to region I and II, where grain and grain boundary effects could be competitive to each other. The sample G1 shown in Fig. 5(a) exhibits three well defined regions separated by the frequency interval of <10.8 kHz, 10.8 kHz–1.4 MHz, and >1.4 MHz. As reported by Abrantes *et al.*,[37] the low frequency region corresponds to dielectric response from electrodes. The medium and high frequency regions are attributed to the grain boundary and grain contributions, respectively. For the sample G1, the electrode and grain boundary contributions to the impedance dominate over the grain contribution. Interestingly, at 223 K the grain contribution to the impedance has increased substantially compared to the contribution at 323 K. Subsequently, the electrode and grain boundary contributions have decreased as shown in the inset of Fig. 5(a). This feature is more pronounced in sample G3 shown in Fig. 5(b) where the frequency intervals for these transitions are not clearly seen. Finally, for sample G5, the grain contribution dominates over the grain boundary while the electrode contribution is suppressed at both 323 and 223 K as shown in Fig. 5(c). Overall, in the high temperature regime, the grain boundary effect dominates over the grain effect. These features suggest that the low temperature dielectric relaxation originates from the grain, whereas at high temperature, relaxation originates from the interfacial grain boundary capacitance effect. Note that the magnitude of these effects depends on the stoichiometry and valence states of the ions in the samples.

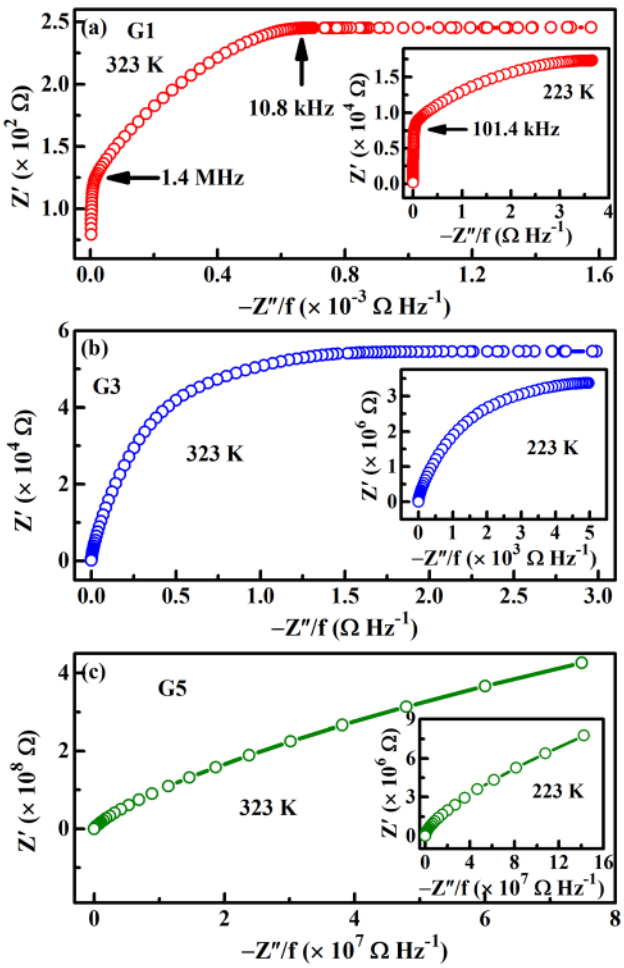

FIG. 5. Plot of Z' versus $-Z''/f$ at 323 K for samples (a) G1, (b) G3, and (c) G5. The inset of each figure shows the respective plot at 223 K.

To get more insight in to the several contributions to the impedance, $-Z''$ versus Z' plots known as the Nyquist plot at different temperatures for G1, G3, and G5 are shown in Figs. 6(a), 6(b) and inset of 6(b), respectively. The sample G1 [see Fig. 6(a)] exhibits two depressed semi-circular arcs at all temperatures. These depressed semicircles suggesting the departure from ideal Debye type behaviour. However, a clear inspection reveals the low frequency arc (≤204 kHz) for 243 K may consist of two overlapped arcs in the frequency regions ≤3.5 kHz and 3.5 kHz ≤ f ≤ 204 kHz. To extract the relevant resistance and capacitance values, plots are fitted using the equivalent circuit consisting of three parallel RC circuits connected in series. The fitted data are shown as the solid line in Fig. 6(a). As proposed earlier, these arcs represent the electrode interface, grain boundary interface, and grain contributions, respectively, with increase in the order of frequency. However, sample G3 shows a single depressed arc which is fitted [solid line in Fig. 6(b)] with an equivalent circuit consists of series combination of two parallel RC circuits. The fitting of the experimental data reveals the grain boundary and grain contribution without any significant electrode interface contribution. This strongly indicates the better insulating character of sample G3 as compared to G1. Similar features are observed for sample G5, but with dominant grain contribution and suppressed grain boundary effect.

To explore it further, the dc conductivity (σ_{dc}) values corresponding to grain and grain boundaries are plotted as a function of 1000/T in Figs. 6(c) and 6(d), respectively, for all samples. The plots show the σ_{dc} for both grain and grain boundary decreases with decrease in temperature due to the insulating behaviour of the samples. In addition, σ_{dc} shows a decreasing trend from G1 to G5, i.e., with increase in annealing time. The activation energies calculated by fitting the data at the high temperature regime using the equation $\sigma_{dc}T = \sigma_0 \exp\left(-\frac{E_a}{k_B T}\right)$ are tabulated in Table II. The obtained E_a values reconfirm that the small polaron hopping mechanism is indeed responsible for the relaxation process in the grain and grain boundary interface.[15,32,36] The increase in E_a with annealing time has a direct correlation with samples attaining a better insulating character with increase in annealing time. This trend could be attributed to the decrease in Mn^{4+} ions and as a consequence, reduction in small polaron hopping between the localized sites (Mn^{3+} and Mn^{4+} states).

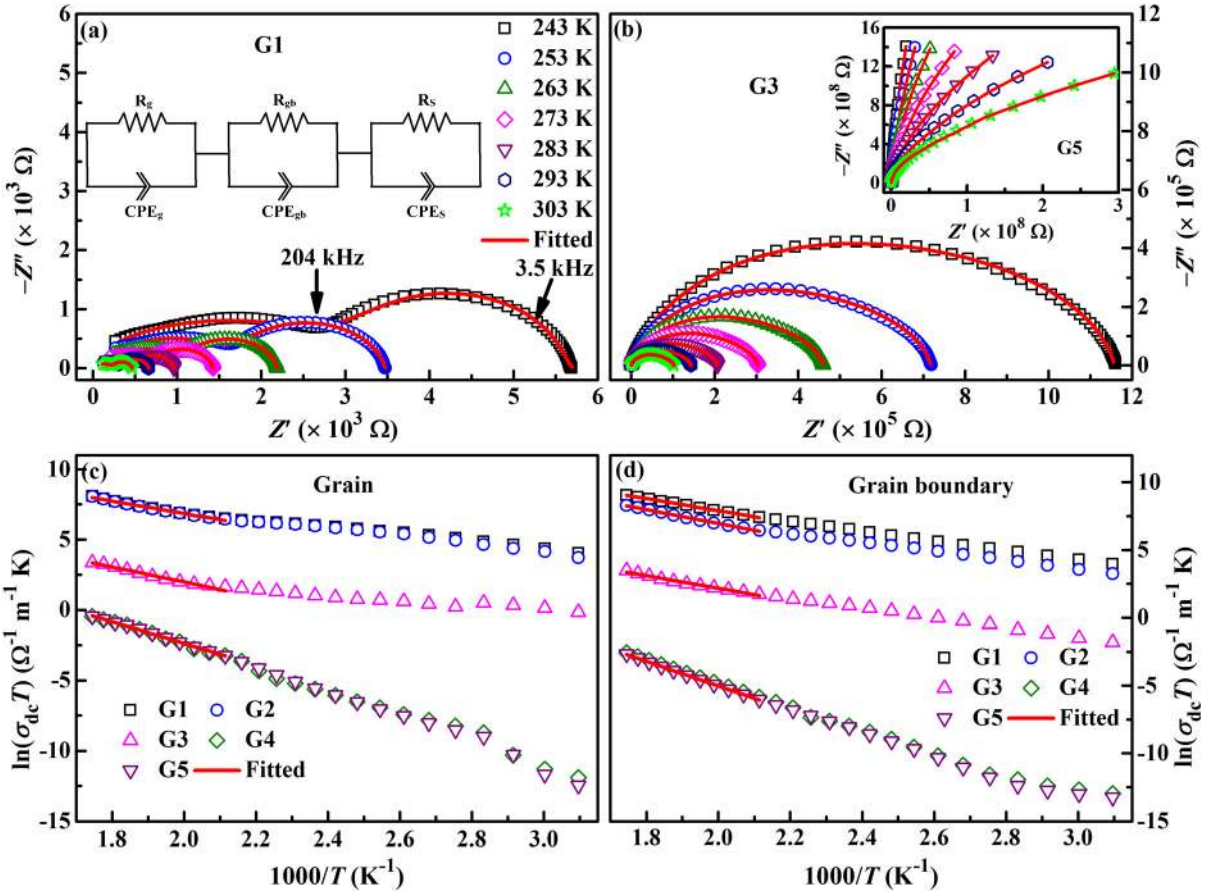

FIG. 6. (a) and (b) Nyquist plots at different temperatures for samples G1 and G3, respectively, (c) and (d) plot of $\ln(\sigma_{dc}T)$ versus $1000/T$ for all samples with linear fitting using the small polaron hopping model for grain and grain boundary contribution, respectively. The inset shows the Nyquist plots at different temperatures for sample G5.

Therefore, it is noteworthy that, the Mn^{3+}/Mn^{4+} ratio in the present samples governs the various electronic properties. The increase in the ratio from sample G1 to G5 makes the sample more insulating with a clear NTCC region appearing towards stoichiometric compounds. The higher Mn^{4+} content brings out different relaxation mechanisms in dielectric and impedance spectra which could otherwise be suppressed along with the dielectric loss by enhancing the Mn^{3+}/Mn^{4+} ratio from G1 to G5.

F. Magnetic properties

To understand the effect of forming gas annealing and the related oxygen non-stoichiometry on the magnetic properties of the samples, the temperature dependent magnetization (M) is measured in field cooled (FC) and zero-field cooled (ZFC) conditions at 100 Oe. The respective plots are shown in Figs. 7(a)–7(d). Though the samples are expected to show the AFM character, the plots did not reveal a clear transition from the paramagnetic (PM) to AFM state due to the masking effect of the high paramagnetic signal from Gd^{3+} moments.[14,22] Nevertheless, M is gradually decreased from G1 to G5 at all temperatures which can be correlated to the decrease in the effect of DE interaction involving Mn^{3+} and Mn^{4+} ions as will be discussed later. To obtain the effective paramagnetic moment (μ_{eff}) and Curie temperature (θ_C) from the Curie-Weiss law,[19] the inverse of magnetic susceptibility ($1/\chi$) is plotted as a function of T measured under the ZFC condition. The representative plot for G2 is shown in the inset of Fig. 7(b). The extracted μ_{eff} and θ_C values are given in Table III. As inferred from the table, the μ_{eff} value is increased with annealing time which is in agreement with the lower magnetic moment of Mn^{4+} (3.87 μ_B) than Mn^{3+} (4.9 μ_B). On the other hand, the theoretical μ_{eff} value of the stoichiometric GMO sample calculated from the formula $\mu_{eff} = \sqrt{(\mu_{Gd})^2 + (\mu_{Mn})^2}$ where, μ_{Gd} and μ_{Mn} are the magnetic moments of Gd^{3+} (7.94 μ_B) and Mn^{3+} (4.9 μ_B), respectively, is 9.33 μ_B. Note that the experimental μ_{eff} value of sample G5 is nearly matching with the theoretical value. Keeping in view of the value of magnetic moment of Mn^{4+} and Mn^{3+}, the observed μ_{eff} values strongly suggest

TABLE II. Activation energy for dc conductivity corresponding to grain and grain boundary obtained from the small polaron hopping mechanism.

	E_a (eV)	
Sample	Grain	Grain boundary
G1	0.37	0.39
G2	0.38	0.41
G3	0.46	0.46
G4	0.67	0.77
G5	0.67	0.78

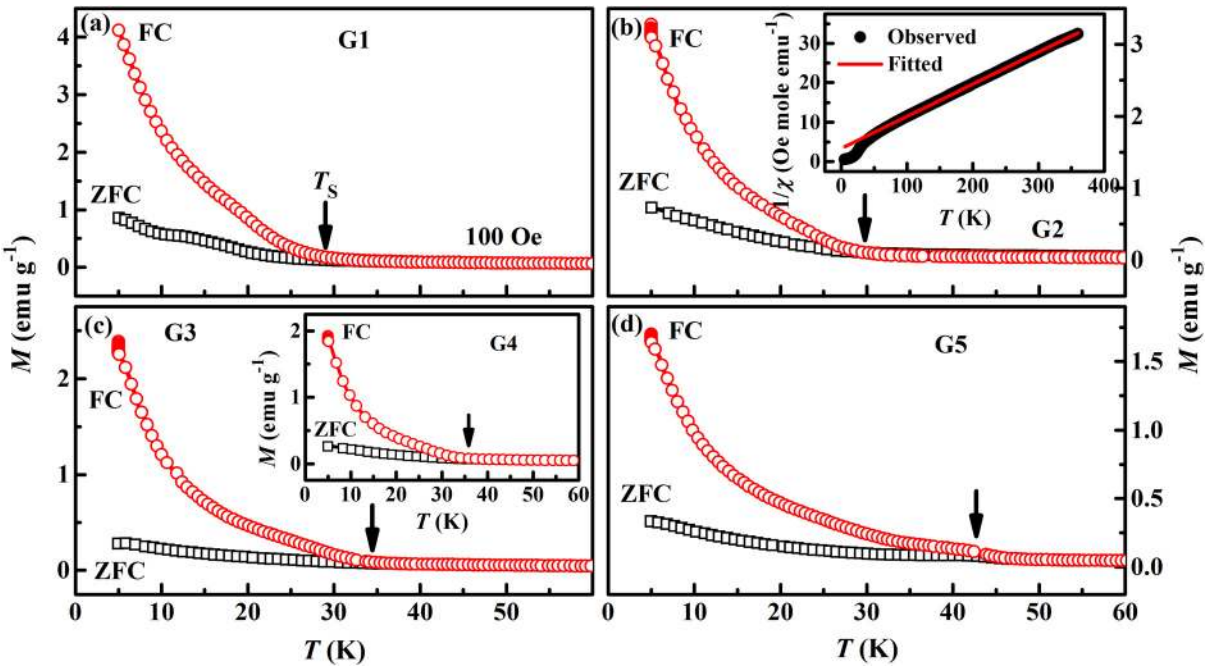

FIG. 7. Temperature dependence of magnetization at 100 Oe field for samples (a) G1, (b) G2, (c) G3, and (d) G5. The inset of (c) shows the respective plot for sample G4 and the inset of (b) shows the linear fitting of the plot $1/\chi$ versus T for sample G2 using the Curie-Weiss law.

that the sample G5 approaches near stoichiometry. A similar trend is observed for θ_C.

The M–T data show that the FC plot deviates from ZFC below a certain temperature and the corresponding temperature is marked as T_S in the graph. The T_S may correspond to the onset of weak ferromagnetism caused by the collinear to canted AFM transition.[22,38–40] The T_S is found to increase from 28 K to 42 K for G1 to G5 and coincides with T_N (42 K) (see Table III). Unlike the expected PM to AFM transition at T_N in single crystalline GMO,[7,8] the sample G5 shows PM to a weak ferromagnetic (WFM) transition at T_N. The observed magnetic features can be discussed with respect to the Mn^{3+}-Mn^{3+} superexchange (SE) interaction, the JT effect of Mn^{3+} ions, and the Mn^{3+}-Mn^{4+} DE interaction.

To understand it further, the M versus magnetic field (H) measurements are performed at 5, 14, and 32 K on all samples and the results are shown in Figs. 8(a), 8(b), and 8(c), respectively. The plots at 5 K shown in Fig. 8(a) reveal the expected AFM character but mixed with the WFM component resulting from the spin canting induced by spin frustration in the system. However, samples G1 and G2 display maximum remnant magnetization with 'S' shaped M–H curves while the value is decreased for G3, G4, and G5.

TABLE III. Variation of μ_{eff}, θ_C, and T_S for all samples.

Sample	μ_{eff} (μ_B)	θ_C (K)	T_S (K)
G1	8.83	−38.2	28.3
G2	8.9	−38.9	29.9
G3	9.1	−40.4	33.8
G4	9.18	−40.9	36.3
G5	9.25	−41.2	42.4

The observed high remnant magnetization for G1 and G2 could be due to the dominant FM DE interaction between Mn^{3+} and Mn^{4+} over the AFM SE interaction which results in WFM ordering.[18–20] This reiterates the presence of higher Mn^{4+} content in G1 and G2 as compared to other

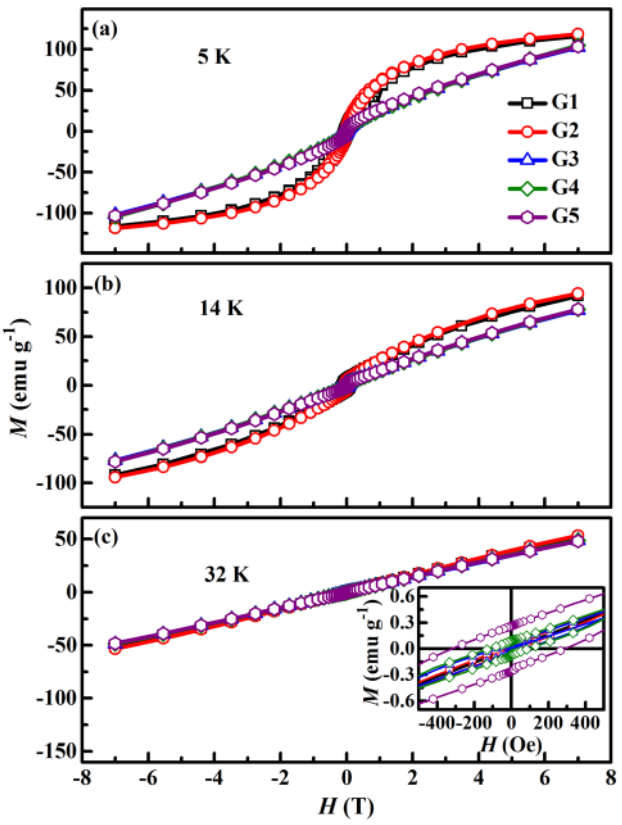

FIG. 8. M-H hysteresis plots for all samples at (a) 5 K, (b) 14 K, and (c) 32 K. The inset shows the enlarged version of the 32 K plots at lower fields.

samples. The observed reduced remnant magnetization in other samples is the consequence of a low Mn^{4+} content and hence a weak DE interaction. The gradual decrease in M observed in the M–T measurements for G1 to G5 shown in Fig. 7 can be correlated to the difference in DE interaction strength with change in the Mn^{3+}/Mn^{4+} ratio.[18,20] A similar trend in remnant magnetization is observed for all samples at 14 K.

However, the trend is reversed at 32 K as shown in Fig. 8(c), and the enlarged version of the loops in the inset. This is in accordance with the observed T_S in M–T plots. For $T_S < 32$ K (G1 and G2), the M–H plots at 32 K show collinear AFM ordering whereas for $T_S > 32$ K (G3, G4, and G5), the M–H plot shows the WFM state (see the inset). Note that the strong Mn^{3+}-Mn^{3+} SE interaction suppresses the weak Mn^{3+}-Mn^{4+} DE interaction for G3, G4, and G5 samples. In addition, it can be seen that the JT effect of Mn^{3+} ions and the associated structural distortion will increase with increase in the amount of Mn^{3+} ions in the samples. In other words, the spin canting may be induced in the system due to JT distortion which in turn results in the observed WFM characteristics as seen in M–H plots for samples G3, G4, and G5. Note that the WFM nature is prominently visible in G5 at 32 K as the measurement temperature is well below T_S (42 K) as compared to the other samples. However, further measurements are necessary to understand the different magnetic phases and spin structures in detail.

IV. CONCLUSIONS

To summarize, we have presented a systematic study on the role of cationic vacancies on the dielectric, impedance, and magnetic properties of $GdMnO_3$ bulk samples. Samples of reduced cationic vacancies and even near stoichiometric compositions are achieved by annealing in a oxygen reduced forming gas atmosphere for different annealing times. XRD and the extracted lattice parameters from Rietveld refinement strongly suggest the presence of Mn^{4+} in the system while XPS confirms the increase of the Mn^{3+}/Mn^{4+} ratio with annealing time. The dielectric spectra reveal various relaxations whose temperature regimes change with cationic vacancies (forming gas annealing time). The activation energy calculated from the conductivity data suggests that the dielectric relaxations can be attributed to either trapped charges from localized Mn-sites (low temperature) or small polaron hopping between Mn^{3+}-Mn^{4+} inside the grain (intermediate temperature) and from the grain boundary interface (high temperature). We believe that the competition between two relaxation mechanisms introduced the negative temperature coefficient of conductivity. Interestingly, magnetic studies demonstrate systematic change in magnetic ordering temperatures with decrease in Mn^{4+} ions in the system. A possible magnetic phase change due to competition between various magnetic interactions is predicted in the system. Overall, the gradual enhancement in the insulating antiferromagnetic character with reduction in cationic vacancy suggests a possible way to modify the electrical and magnetic states of polycrystalline $GdMnO_3$.

ACKNOWLEDGMENTS

This work was supported by DST-SERB under the sanction order No. EMR/2016/002370. The authors thank Professor P. N. Santhosh, IIT Madras, for providing the facilities for sample preparation.

[1]M. Kenzelmann, A. B. Harris, S. Jonas, C. Broholm, J. Schefer, S. B. Kim, C. L. Zhang, S.-W. Cheong, O. P. Vajk, and J. W. Lynn, Phys. Rev. Lett. **95**, 087206 (2005).
[2]I. A. Sergienko and E. Dagotto, Phys. Rev. B **73**, 094434 (2006).
[3]J. Magesh, P. Murugavel, R. V. K. Mangalam, K. Singh, C. Simon, and W. Prellier, J. Appl. Phys. **118**, 074102 (2015).
[4]S. Jin, T. H. Tiefel, M. McCormack, R. A. Fastnacht, R. Ramesh, and L. H. Chen, Science **264**, 413 (1994).
[5]R. V. Helmolt, J. Wecker, B. Holzapfel, L. Schultz, and K. Samwer, Phys. Rev. Lett. **71**, 2331 (1993).
[6]B. Garcia-Landa, J. M. D. Teresa, and M. R. Ibarra, J. Appl. Phys. **83**, 7664 (1998).
[7]T. Kimura, G. Lawes, T. Goto, Y. Tokura, and A. P. Ramirez, Phys. Rev. B **71**, 224425 (2005).
[8]T. Aoyama, A. Iyama, K. Shimizu, and T. Kimura, Phys. Rev. B **91**, 081107(R) (2015).
[9]G. J. Snyder, C. H. Booth, F. Bridges, R. Hiskes, S. DiCarolis, M. R. Beasley, and T. H. Geballe, Phys. Rev. B **55**, 6453 (1997).
[10]P. Murugavel, J. H. Lee, J.-G. Yoon, T. W. Noh, J.-S. Chung, M. Heu, and S. Yoon, Appl. Phys. Lett. **82**, 1908 (2003).
[11]P. Schiffer, A. P. Ramirez, W. Bao, and S.-W. Cheong, Phys. Rev. Lett. **75**, 3336 (1995).
[12]S. Z. Li, T. T. Wang, H. Q. Han, X. Z. Wang, H. Li, J. Liu, and J.-M. Liu, J. Phys. D: Appl. Phys. **45**, 055003 (2012).
[13]P. Mandal, V. S. Bhadram, Y. Sundarayya, C. Narayana, A. Sundaresan, and C. N. R. Rao, Phys. Rev. Lett. **107**, 137202 (2011).
[14]A. Pal, C. Dhana Sekhar, A. Venimadhav, and P. Murugavel, J. Phys.: Condens. Matter **29**, 405803 (2017).
[15]W. Khan, A. H. Naqvi, M. Gupta, S. Husain, and R. Kumar, J. Chem. Phys. **135**, 054501 (2011).
[16]J. A. M. V. Roosmalen, E. H. P. Cordfunke, R. B. Helmholdt, and H. W. Zandbergen, J. Solid State Chem. **110**, 100 (1994).
[17]J. A. Alonso, M. J. Martinez-Lope, M. T. Casais, J. L. MacManus-Driscoll, P. S. I. P. N. De Silva, L. F. Cohen, and M. T. Fernandez-Diaz, J. Mater. Chem. **7**, 2139 (1997).
[18]W. S. Choi, Z. Marton, S. Y. Jang, S. J. Moon, B. C. Jeon, J. H. Shin, S. S. A. Seo, T. W. Noh, K. Myung-Whun, H. N. Lee, and Y. S. Lee, J. Phys. D: Appl. Phys. **42**, 165401 (2009).
[19]P. Tiwari and C. Rath, J. Magn. Magn. Mater. **441**, 635 (2017).
[20]H. Khanduri, M. C. Dimri, S. Vasala, S. Leinberg, R. Lohmus, T. V. Ashworth, A. Mere, J. Krustok, M. Karppinen, and R. Stern, J. Phys. D: Appl. Phys. **46**, 175003 (2013).
[21]A. Pimenov, A. A. Mukhin, V. Y. Ivanov, V. D. Travkin, A. M. Balbashov, and A. Loidl, Nat. Phys. **2**, 97 (2006).
[22]L. Lin, L. Li, Z. B. Yan, Y. M. Tao, S. Dong, and J.-M. Liu, Appl. Phys. A **112**, 947 (2013).
[23]X. L. Wang, D. Li, T. Y. Cui, P. Kharel, W. Liu, and Z. D. Zhang, J. Appl. Phys. **107**, 09B510 (2010).
[24]G. Q. Zhang, S. J. Luo, S. Dong, Y. J. Gao, K. F. Wang, and J.-M. Liu, J. Appl. Phys. **109**, 07D901 (2011).
[25]L. Li, L. Lin, Z. B. Yan, Q. Y. He, and J.-M. Liu, J. Appl. Phys. **112**, 034115 (2012).
[26]X. Zhang, Y. G. Zhao, Y. F. Cui, L. D. Ye, D. Y. Zhao, P. S. Li, J. W. Wang, M. H. Zhu, H. Y. Zhang, and G. H. Rao, Appl. Phys. Lett. **104**, 062903 (2014).
[27]A. Pal, C. Dhana Sekhar, A. Venimadhav, W. Prellier, and P. Murugavel, J. Appl. Phys. **123**, 014102 (2018).
[28]M. Yahia and H. Batis, Eur. J. Inorg. Chem. **2003**, 2486.
[29]V. Cuartero, J. Blasco, G. Subias, J. Garcia, C. Meneghini, and G. Aquilanti, Phys. Rev. B **92**, 125118 (2015).
[30]P. R. Mandal and T. K. Nath, J. Alloys Compd. **628**, 379 (2015).
[31]N. F. Mott and E. A. Davis, *Electronic Processes in Non-Crystalline Materials* (Clarendon Press, Oxford, England, 1971).
[32]C. Ganeshraj, S. Kavita, R. Mahendiran, N. Sharma, A. Das, and P. N. Santhosh, Appl. Phys. Lett. **103**, 112909 (2013).

[33]S. Bhattacharya, D. K. Modak, P. K. Pal, and B. K. Chaudhuri, Mater. Chem. Phys. **68**, 239 (2001).
[34]B. Dabrowski, K. Rogacki, X. Xiong, P. W. Klamut, R. Dybzinski, J. Shaffer, and J. D. Jorgensen, Phys. Rev. B **58**, 2716 (1998).
[35]I. G. Austin and N. F. Mott, Adv. Phys. **18**, 41 (1969).
[36]C. C. Wang, Y. M. Cui, and L. W. Zhang, Appl. Phys. Lett. **90**, 012904 (2007).
[37]J. C. C. Abrantes, J. A. Labrincha, and J. R. Frade, Mater. Res. Bull. **35**, 727 (2000).
[38]W. Hong-Tao, Z. Tong, H. Bo, T. Qian, and X. Zhu-An, Chin. Phys. Lett. **28**, 027501 (2011).
[39]M. Staruch, G. Lawes, A. Kumarasiri, L. F. Cotica, and M. Jain, Appl. Phys. Lett. **102**, 062908 (2013).
[40]M. E. Amrani, M. Zaghrioui, V. T. Phuoc, F. Gervais, and N. E. Massa, J. Magn. Magn. Mater. **361**, 1 (2014).